Localized plasmonic heating for single-molecule DNA rupture measurements in optical tweezers

Prerna Kabtiyal[1], Ariel Robbins[2], Elizabeth Jergens[2], Carlos E. Castro[2,3], Jessica O. Winter[2,4], Michael G. Poirier[1,2,5]*, Ezekiel Johnston-Halperin[1]**

[1]Department of Physics, The Ohio State University, Columbus, Ohio-43210, USA

[2] Biophysics Graduate Program, The Ohio State University, Columbus, Ohio-43210, USA

[3] Department of Mechanical and Aerospace Engineering, The Ohio State University, Columbus, Ohio-43210, USA

[4]Department of Chemical and Biomolecular Engineering, The Ohio State University, Columbus, Ohio-43210, USA

[5]Department of Chemistry and Biochemistry, The Ohio State University, Columbus, Ohio-43210, USA

*poirier.18@osu.edu , **johnston-halperin.1@osu.edu

Abstract: To date, studies into the thermodynamic and kinetic processes that underlie biological function and nanomachine actuation in biological and biology-inspired molecular constructs have primarily focused on photothermal heating of ensemble systems, highlighting the need for probes that are localized within the molecular construct and capable of resolving single-molecule response. Here we present an experimental demonstration of wavelength-selective, localized heating at the single-molecule level using the surface plasmon resonance of a 15 nm gold nanoparticle (AuNP). Our approach is compatible with force-spectroscopy measurements and can be applied to studies of the single-molecule thermodynamic properties of DNA origami nanomachines as well as biomolecular complexes. We further demonstrate wavelength-selectivity and establish the temperature dependence of the reaction coordinate for base-pair disruption in the shear-rupture geometry, demonstrating the utility and flexibility of this approach for both fundamental studies of local (nanometer-scale) temperature gradients and for rapid and multiplexed nanomachine actuation.

Keywords: Plasmonic heating, force spectroscopy, single-molecule, DNA, optical tweezers

Localized temperature control at the nanoscale has emerged as an important field of research owing to its varied applications in the study of biological systems[1,2,3], biomedicine[4,5,6,7], photothermal chemistry[8], light to heat conversion[9,10], and nano-machine/nano-assembly actuation[11,12], with temperature-dependent studies at the single-molecule level being of particular interest[13,14,15,16,17]. Imaging and dynamic measurements at the single molecule level can provide a more in depth understanding of biomolecule behavior and real-time dynamics than ensemble measurements[18,19], which necessarily provide averaged parameter values that can obscure the origin of the observed phenomena. Typically, temperature control in these single-molecule studies has been achieved through global manipulation of the environment using, *e.g.*, thermoelectric heating of the objective stage[16,20,21]. One recent study built on this technique to decouple the heat transfer between the objective and sample chamber in magnetic-tweezers setup, accomplishing sample heating with short time intervals and wide temperature range[22]. Other recently developed heating approaches primarily rely on use of near-infrared (NIR) laser heating, both directly[17,23,24,25,26,27,28] and indirectly[29,30]. Direct techniques exploit the absorption of NIR light by the water molecules in the excited volume, whereas the indirect techniques rely on the deposition of an absorptive layer on the flow cell to localize laser induced heating. However, the length scale of this localization is still relatively large compared to the systems of interest, typically heating picolitre volumes (1000 μm^3)[23,28]. This approach can be pushed to the diffraction limit, as shown in a recent report where localized heating at the sub-cellular scale (a ~5μm diameter heat spot with sub-picolitre volume) was generated in a live cell to impact cellular functions[31]. However, to date none of these approaches allow heating at the nanometer length scales that are relevant for probing and manipulating molecular function.

Here we present and experimentally validate an approach to nanometer-scale temperature control at the single molecule level through the resonant plasmonic heating of gold nanoparticles[2,3] localized to a targeted region of a molecular construct. It is compatible with single-molecule force spectroscopy measurements, overcomes the challenges associated with conventional temperature dependent studies, and is straightforward to implement in DNA nanomachines and for dynamic thermal studies of a wide variety of molecular

structures/nanomachines[32,33,34]. Further, the wavelength-sensitivity of this approach has the potential to dynamically create and modify multiple temperature profiles within one construct through, *e.g.*, multiplexed excitation energies and variable intensity.

This functionality is experimentally demonstrated through the systematic study of plasmonic excitation assisted shear-induced DNA rupture under constant force (Fig. 1a). The DNA base pair attachments are

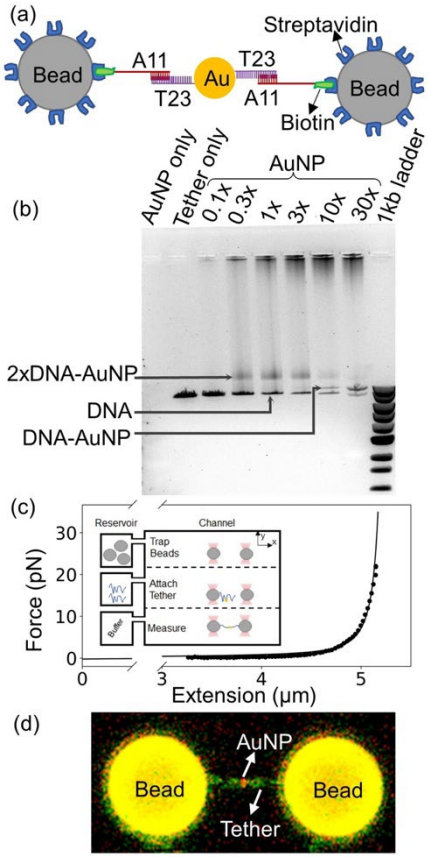

Figure 1: (a) Schematic of A11-Au-A11 tether attachment between Streptavidin coated polystyrene beads trapped in optical traps; **(b)** Electrophoresis gel showing A11-Au-A11 conjugation yield for different Au:A11 concentrations; **(c)** Force-extension data for A11-Au-A11 tether attached between two beads[dots] fit to WLC model[line] confirming single-tether attachment (inset: schematic of the experimental procedure in the C-Trap flow cell); **(d)** Fluorescence image of the Bead-A11-Au-A11- Bead composite labelled with sytox orange (green) and cy5 (red).

destabilized due to a localized temperature increase generated from a neighboring excited gold nanoparticle, reducing the DNA rupture time under a given applied force.

Rupture time measurements are made through single molecule force spectroscopy conducted in a dual-trap optical tweezers instrument equipped with confocal laser excitation and single molecule fluorescence detection (Lumicks C-Trap). The structure under study consists of a central AuNP that is attached to two dsDNA tethers through polyA-polyT strand conjugation (Fig. 1a). This places the polyA-polyT construct in the vicinity of the AuNP, allowing it to be locally heated through AuNP excitation. The other ends of the dsDNA strands are terminated with biotin to enable selective attachment to streptavidin-functionalized polystyrene beads that serve as handles in the dual-trap optical tweezers setup.

The experimental realization of this structure begins with the selection of the central gold nanoparticle (AuNP). The goal is to choose a size that ~~maximizes~~ enables high light to heat conversion ratio, which is defined by the competition between the absorbed energy and scattered energy. As the AuNP diameter increases the increase in surface area allows more light to be absorbed but also leads to an increase in scattering[35]. Prior theoretical results[35] were extrapolated to calculate the absorption cross-section for 15nm AuNPs to be $C_{abs} = (0.990 \times 10^{-15}\,m^2)$ at the nanoparticle plasmon resonance of 520 nm, indicating that this nanoparticle size has sufficient absorption cross section to serve as a localized, optically-pumped heat source. To enable attachment to the DNA tether the nanoparticles are functionalized with 23 base poly-thymine (T-23) ssDNA oligonucleotides through a carbon chain linker using thiol attachment (purchased commercially through Nanopartz Inc.). Following common practice for the attachment of gold nanostructures to DNA structures[37,38,39,40], a T-23 oligonucleotide was chosen to coat the AuNP. This allows for more uniform coverage of the nanoparticle surface compared to oligonucleotides with A, C, G bases due to their higher binding affinity with Au, which inhibits even coverage and leads to agglomeration on the Au surface[36].

The dsDNA tethers shown in Fig. 1a are generated from restriction enzyme digestion of a circular plasmid DNA(pPSU2) that generates a 4 base 5' overhang. Following this, two DNA oligonucleotides are ligated to one end that introduces an 11 base polyadenine (A-11) ssDNA 5' extension that can then base pair to T-23 oligos that are functionalized to the AuNP. The opposite DNA end is ligated to two DNA oligonucleotides to introduce a biotin molecule at this end, which binds a streptavidin coated polystyrene bead that

provides a handle for the optical trap. The attachment of AuNPs to the dsDNA tethers is done through an annealing process where T-23 coated AuNPs and dsDNA tethers with A-11 overhangs are incubated at 55 ºC for 10 minutes followed by a linear temperature reduction to 4 ºC in 45 minutes. The relative concentration of the dsDNA tether to the AuNPs were optimized for the attachment of two dsDNA tethers to a single AuNP (Fig. 1a). In addition, the presence of longer poly-thymine strands (T-23) compared to the shorter poly-adenine strands (A-11) provides multiple attachment positions along the T-23 strand where A-11 is fully base paired and therefore enhances the conjugation probability and yield of the self-assembly process.

The final optimally assembled AuNP:tether construct is introduced into a multi-channel microfluidic flow cell for conjugation to two polystyrene beads (Fig. 1c, inset). The microfluidic flow cell has five laminar flow channels, which allows for the optical trap to move between channels to iteratively assemble bead-DNA-AuNP-DNA-bead structures. The assembly protocol starts with two polystyrene beads optically trapped in the "beads channel", followed by the attachment of a DNA-Au-DNA conjugate between the two beads in the "tether channel". The whole assembly is then moved to the buffer channel (0.5xTE+100mM NaCl+5.5mM $MgCl_2$+0.05% Tween20) where one of the traps is moved to adjust the apply force on the construct. Once the assembly is formed, it is important to ensure the presence of a single DNA-AuNP-DNA conjugate between the two trapped beads, as the presence of multiple conjugates will lead to misleading measurements (multiple conjugates in parallel require significantly higher force to rupture). Single tether conjugation is confirmed through comparison of the measured force *vs.* extension curve with the worm-like chain (WLC) model[41], as shown in Fig. 1c, before proceeding to photothermal measurements.

The configuration of the assembled structure is further validated using single molecule confocal fluorescence microscopy to image the DNA tether and the AuNP while it is suspended between the two beads that are held by the optical traps. For these studies, the assembled structure is transferred to a flow channel that contains Cy5 fluorophore-labeled polyA oligos (A12:cy5) and sytox orange (DNA binding fluorophore) (Fig. 1c, inset). During the incubation in this flow channel, the A12:cy5 oligos attach to the T23 oligos on the AuNP and the sytox orange molecules bind to the two DNA tethers.

Simultaneous scanning with 561 nm and 639 nm laser excitation generates a fluorescence image of the assembled construct shown in Fig. 1d, confirming construct conformation. This image additionally confirms the AuNP position relative to the two DNA handles and two beads for later confocal plasmonic excitation that capitalizes on the high spatial resolution of the C-Trap instrument (350 nm).

The dynamic response to thermal excitation under a constant shear-force is studied by exciting the AuNP with a diffraction-limited confocal laser until rupture. Executing this measurement approach requires a DNA construct that has a resident time at room temperature on timescales longer than our measurement, but susceptible to rupture at temperatures accessible by laser-induced heating. A previous study that reports DNA oligonucleotide resident times as a function of length[42] informed the choice of using a poly-A length of A-11. This length choice was confirmed by the observation that stable single tethers could be reproducibly captured in the dual optical trap.

Next, to investigate the feasibility of thermal induced poly-A release from the AuNP, the temperature change in the vicinity of the AuNP can be calculated from the time-independent heat transfer equation[43],

$$\Delta T(r) = \frac{C_{abs} I}{4\pi k r} \qquad (1)$$

where, ΔT is the temperature difference from ambient temperature, C_{abs} is the absorption cross-section at excitation wavelength, I is the laser fluence, k is the thermal conductivity of water and r is the distance from the center

of the AuNP (valid for values of r larger than

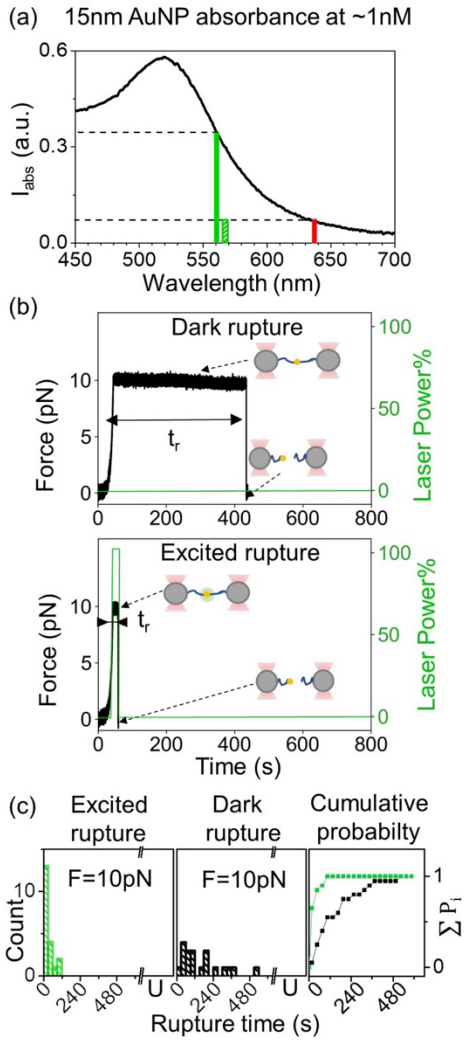

Figure 2: (a) Absorption spectrum for a 15 nm gold nanoparticle; **(b)** Force vs time plots for an instance of excited rupture time vs dark rupture time, U represents instances where tether remained unruptured at >600s; **(c)** Comparison of dark ruptures and excited ruptures (N=20, bin width=30s) at 10pN for KS hypothesis test.

the radius of the AuNP).

In order to calculate ΔT for these experimental conditions, it is necessary to modify literature values of resonant plasmonic excitation[35] to reflect the excitation wavelength of 561 nm. This correction is determined from the absorption spectrum of a suspension of the 15 nm AuNPs (1 nM) shown in Fig. 2a, revealing a decrease in absorption to 48.3% of the resonant peak. Based on this value, a confocal laser spot at a wavelength of 561 nm and with power of 47.9 μW is predicted to raise the temperature to an average of 34.1 °C over a distance of 0.5 nm to 11.9 nm from the AuNP surface (the length of the polyA-polyT construct). The efficacy of this temperature increase in promoting rupture is experimentally evaluated by a comparison between tether rupture times observed for a dark (no laser excitation) rupture events and laser-excited rupture events (Fig. 2b). The force is gradually ramped to a value of 10 pN, then held constant until tether rupture, defining a rupture time, t_r. For the plasmonic heating studies the laser is turned on when the force reaches 10 pN. This single-shot comparison reveals roughly an order of magnitude difference in rupture time, suggesting that localized melting has been achieved, warranting a more comprehensive and systematic investigation of the heating and rupture process.

To establish the statistical significance of the plasmonically heated

shear-induced rupture, multiple independent events (n=20) of excited and dark ruptures are compared at an applied shear-force of 10 pN, as shown in the left two panels of Fig. 2c. The observed distributions of rupture times in the two experiments (dark *vs.* light) appear quite distinct, with a much broader distribution in times observed for the dark rupture experimental protocol. The Kolmogorov-Smirnov (KS) two-sample hypothesis test is used to statistically test the hypothesis that the two distributions belong to different processes. The right panel of Fig. 2c shows the cumulative probability of rupture for both dark (black curve) and excited (green curve) measurement conditions. A comparison of the maximum deviation between the two cumulative probability curves (KS statistic) to the Kolmogorov distribution table is used to extract a *p*-value, where $p = 1$ indicates identical distributions arising from the same underlying probability distribution and $p < 0.05$ is accepted as the statistically significant threshold for demonstrating that two distributions arise from distinct underlying probability distributions[44]. The KS analysis of the data presented in Fig. 2c yields $p = 0.0015$, indicating a high level of confidence that the plasmonic heating induces a statistically significant change in the rupture probability.

Varying the wavelength of the laser excitation provides an important cross-check to distinguish between the localized thermal excitation model described above and other potential mechanisms such as excitation and degradation of chemical bonds in the tethers or attachment chemistry. Figure 2a shows the substantial decrease in absorption for a wavelength of 639nm (7.7% of the resonant plasmon absorption, or roughly 6x lower than excitation at 561nm), providing the opportunity to compare the predicted thermal excitation for this lower-energy excitation in comparison to the measurements at 561 nm described in Fig. 2c. Further, as the excited state temperature profile approaches the critical rupture temperature of the relevant oligos under these force loading conditions it becomes important to consider the various possible conformations available for a given tether as, *e.g.,* the A11 overhang can attach at various points along the T23 oligo (A11-T11 construct placement varying from 0.5 nm to 11.9 nm from the AuNP surface). This variation is shown schematically at the top of Fig. 3a for a fully stretched DNA construct and is compared to the spatially dependent temperature profiles calculated using Eq. (1). This comparison should be considered a

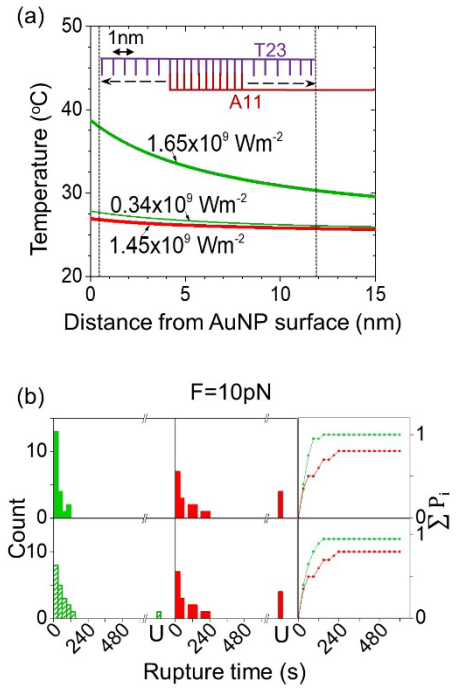

Figure 3: (a) Calculated Temperature profile around the AuNP for 561nm(P=100% [green bold] , 20.6% [green thin]) and 639nm(P=100% [red bold]); **(b)** Comparison of rupture times (N=20) at F=10pN for different powers and wavelengths: comparison between comparable incident intensities of green and red laser [top panel] and comparable absorbed intensities of green and red laser [bottom panel], U represents instances that remained unruptured for more than 600s. Right panel: outcome of the KS test comparing red rupture to green rupture at comparable incident intensity ($D_s > D_{crit}^{\alpha=0.05}$) [upper panel] and with comparable absorbed intensity ($D_s < D_{crit}^{\alpha=0.05}$) [lower panel].

worst-case estimate, as the end-to-end length of the single-stranded portions of the construct will depend on the force loading, with shorter distances (and consequently higher average temperature) at lower force. Using the baseline of the 561 nm excitation used for the measurements presented in Fig. 1 for comparison and an incident power of 46μW at 639 nm provided by the C-Trap, Eq. (1) yields a temperature profile that varies from 26.9 °C at the AuNP surface to 25.7 °C at 12 nm (Fig. 3a, red curve). This predicts that the temperature generated from plasmonic heating at an excitation wavelength of 639 nm is substantially lower than that predicted for 561 nm at all distances and shows a smaller absolute variation in temperature with distance. When comparing these distinct temperature profiles to the expected variation in binding position within the T23 oligo, one would anticipate a significant difference in rupture dynamics between the two excitation regimes.

Experimental validation of this prediction is achieved by subjecting individual constructs to a constant shearing force of 10 pN while the AuNP is continuously excited with 639 nm light for up to 600 s and comparing the results to the illumination at 561 nm, Fig. 3b (for the purposes of this experiment, observations are terminated after 600 s and the construct labelled as "unruptured"). The incident fluence for the two excitation wavelengths are comparable, $I_{561nm} = 16.4\text{x}10^{-4}$ μWnm^{-2} and $I_{639nm} = 14.6\text{x}10^{-4}$ μWnm^{-2}, to highlight differences in response due to the predicted

difference in heat transfer efficiency from the excitation light to the nanoparticles. A comparison of shear-force induced rupture times of the DNA-Au-DNA construct when excited with 561 nm (green) and 639 nm (red) can be seen in Fig. 3b. The distribution for the 639 nm is broader and skewed towards the longer rupture times compared to excitation at 561 nm. Critically, even when the total energy present in the excitation beam is comparable, the difference in spectral overlap with the plasmon resonance drives a significant difference in the resulting temperature, and consequently, a difference in rupture time. Further, the existence of unruptured constructs under 639 nm excitation is consistent with the calculation of the induced temperature profile shown in Fig. 3a. The KS two-sample hypothesis test is again applied to test the statistical relevance of the observed difference between the green and red rupture distributions. The KS hypothesis test (Fig 3b, right panel) shows that the two distributions are statistically distinct at the $p = 0.037$ level (3.7% chance of originating from same population).

This hypothesis can be tested further by comparison to a third excitation condition, wherein the flux of 561 nm excitation is reduced so that the *absorbed flux* at 561 nm is comparable to the absorbed flux at 639 nm (*i.e.*, taking into account the reduced absorption cross section at 639 nm; Fig. 2a). This will provide comparable heat flux into the AuNP while the energy per photon is varied (which would be the relevant parameter for resonant excitation). The calculated temperature profile for the low power 561 nm excitation (Fig. 3a, light green curve) is comparable to 639 nm excitation, with slightly higher temperatures (27.8 ºC at AuNP surface and 26.1 ºC at 12 nm). The experimental comparison is shown in the lower panels of Fig 3b, and the low-intensity 561 nm excitation does indeed broaden towards the 639 nm distribution. The KS two-sample hypothesis test concludes that the two sample distributions originate from differing populations at a p-value of $p = 0.33$, implying that there is a 33% chance that the two sample distributions originate from the same population. This is much higher than the 3.7% chance of same population origin as reported above for red versus green excitation at comparable incident fluence. This provides further support for the interpretation that the rupture time distributions are dependent on the plasmonically generated heat flux, and the observed accelerated ruptures are in fact a consequence of heat generation due to plasmonic excitation.

Next, the comparison between excited and dark rupture is used to explore the impact of decreasing shear-force on the rupture times of these DNA-Au-DNA constructs. For this measurement the 10 pN measurements reported above (Fig. 2c) are supplemented by complementary measurements at shearing forces of 5 pN and 2.5 pN. As can be seen from Fig 4, ruptures excited at 561 nm and 5 pN occur at times that are short relative to the measurement window, while the dark rupture distribution shows a significant number of unruptured tethers. The KS test concludes that the dark and excited sample distributions originate from different population distributions at p=0.00011 level, a similar level of confidence to 10 pN. As expected, when the force is further reduced to 2.5 pN the rate of rupture further decreases, with rupture times approaching the available measurement window. As a consequence, the primary difference between the excited and dark rupture distributions is evident in the difference in the fraction of tethers that remain unruptured. This behavior results in the KS test having a lower statistical confidence in their being a difference between the excited and dark rupture distributions (p=0.082 at F=2.5 pN).

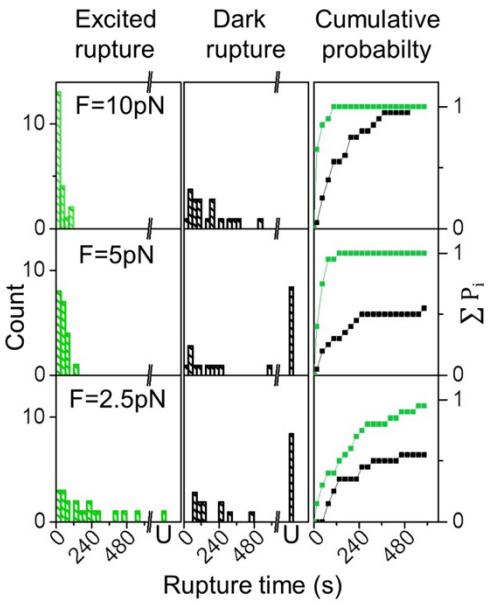

Figure 4: Comparison of Dark ruptures and Excited ruptures (N=20, bin width=30s) at three different forces 2.5pN, 5pN, 10pN. U represents instances that remained unruptured for more than 600s. The right-most column shows the cumulative probability for each force-loading condition, indicating that excited and dark rupture events arise from different underlying probability distributions at high force (10 pN and 5 pN) but become less distinct at low force (2.5 pN), see main text.

These systematic force studies can be used to extract the temperature dependence of the parameters defining the free energy landscape of the relevant DNA rupture dynamics. The rate of shear-induced rupture (k) depends on four parameters: the Gibbs free energy barrier (ΔG), applied force (F), the change in length of the base paired poly-A (d), and temperature (T) in accordance with the Arrhenius equation,

$$k = k_0 e^{\frac{-\Delta G + Fd}{k_B T}} \qquad (2)$$

where k_0 is the Arrhenius constant and k_B is the Boltzmann constant. This equation can also be modified as,

$$\ln(k) = \left[\ln k_0 - \frac{\Delta G}{k_B T}\right] + \frac{Fd}{k_B T} \quad (3)$$

which makes the natural logarithm of k a linear function of applied force F with slope of d/k_BT. To obtain the rupture rate constant for each applied force, the cumulative probability ($\sum P_i$) of binned rupture times is fit to the function $p = 1 - e^{-kx}$ (Supplemental Figure S1) and the linear relationship is plotted at the three forces (F = 2.5 pN, 5 pN, 10 pN) for dark and excited rupture (Supplemental Figure S2). The extracted slope for dark ruptures (T = 25 ºC) and excited ruptures (T = 34.1 ºC) are 0.15 ± 0.04 pN^{-1} and 0.3 ± 0.15 pN^{-1}, respectively. Using the assumption of a temperature-independent change in length, d, these slopes predict a lower temperature at excited rupture as compared to dark rupture, which is not physical for these experimental conditions. Instead, this indicates that the reaction coordinate in the shear-induced rupture of the DNA-Au-DNA construct is temperature dependent and varies from d_{Dark} = (0.62 ± 0.16) nm at ambient temperature of 25 ºC to $d_{Excited}$ = (1.37 ± 0.69) nm at a calculated spatially averaged temperature of 34.1ºC for excitation with 561 nm at 47.9 µW. The room temperature determined d_{Dark} is nearly the same as a previous optical trap measurement to shear a 15 bp DNA molecule[45], which provides further confidence in these calculations. Interestingly, there does not appear to be a report on the temperature dependence of d for shearing DNA. This highlights how the combination of local, modulated thermal excitation with established single-molecule force spectroscopies can provide new temperature dependent information at the single molecule level.

In conclusion, we have demonstrated an experimental strategy for on-demand, wavelength-selective, and localized temperature control at the single-molecule level. We have employed this approach to reveal a previously unreported temperature dependence to the shear-force rupture reaction coordinate that plays an important role in understanding these rupture dynamics. This scheme can be further extended for the study of thermodynamics of other DNA sequences and constructs in place of the polyA-polyT junction studied here, such as DNA-based nanomachines[46], and

biologically relevant folded structures of DNA, RNA, and proteins[47]. Further, it is compatible with other single-molecule force spectroscopies such as magnetic tweezers[48] and atomic-force microscopy[49]. Further, the wavelength sensitivity provides a pathway to the selective addressing of multiple, localized heat sources within a single construct, raising the possibility of complex actuation and more sophisticated thermodynamic studies.

AUTHOR INFORMATION

P.K. developed and conducted the DNA rupture experiments in the C-Trap, analyzed the experimental rupture time data, and performed calculations for extracting the reported temperature-dependent reaction coordinate from the experimental data. A.R. prepared the DNA tethers used for the experiments and optimized processes for conjugation of AuNP to tether.

E.J. prepared oligo-coated AuNPs for preliminary stages of experiment process optimization. C.E.C, J.W., M.G.P., E.J.H. provided regular guidance and advice on various aspects of the project such as sample design and preparation, experiment design & optimization, data analysis, and interpretation of experimental results.

Author emails: Prerna Kabtiyal (kabtiyal.1@osu.edu), Ariel Robbins (robbins.405@osu.edu), Elizabeth Jergens (jergens.8@osu.edu), Carlos E. Castro (castro.39@osu.edu), Jessica Winter (winter.63@osu.edu), Michael G. Poirier (poirier.18@osu.edu), Ezekiel Johnston-Halperin (johnston-halperin.1@osu.edu).

SUPPORTING INFORMATION

Calculation of incident intensities for different wavelengths, calculation of temperature dependent reaction coordinate for dark and excited rupture.

ACKNOWLEDGMENTS

We are grateful to the Johnston-Halperin, Poirier, Castro, and Winter Labs for feedback on this work. This work was supported by the US Department of Energy (DE-SC0017270 to EJH, MGP, CEC, JW). The National Institutions of Health provided support for the C-Trap instrument (S10OD028705 to MGP). The NanoSystems Laboratory provided technical support for the C-Trap instrument.

References

(1) Cognet, L.; Tardin, C.; Boyer, D.; Choquett, D.; Tamarat, P.; Lounis, B. Single Metallic Nanoparticle Imaging for Protein Detection in Cells. *Proc. Natl. Acad. Sci. U. S. A.* **2003**, *100* (20), 11350–11355. https://doi.org/10.1073/PNAS.1534635100/SUPPL_FILE/4635MOV1.MOV.

(2) Reismann, M.; Bretschneider, J. C.; Von Plessen, G.; Simon, U. Reversible Photothermal Melting of DNA in DNA–Gold-Nanoparticle Networks. *Small* **2008**, *4* (5), 607–610. https://doi.org/10.1002/SMLL.200701317.

(3) Stehr, J.; Hrelescu, C.; Sperling, R. A.; Raschke, G.; Wunderlich, M.; Nichtl, A.; Heindl, D.; Kürzinger, K.; Parak, W. J.; Klar, T. A.; Feldmann, S. J. Gold NanoStoves for Microsecond DNA Melting Analysis. *Nano Lett.* **2008**, *8* (2), 619–623. https://doi.org/10.1021/NL073028I/ASSET/IMAGES/LARGE/NL073028IF00003.JPEG.

(4) Skirtach, A. G.; Dejugnat, C.; Braun, D.; Susha, A. S.; Rogach, A. L.; Parak, W. J.; Möhwald, H.; Sukhorukovt, G. B. The Role of Metal Nanoparticles in Remote Release of Encapsulated Materials. *Nano Lett.* **2005**, *5* (7), 1371–1377. https://doi.org/10.1021/NL050693N/SUPPL_FILE/NL050693NSI20050414_035917.AVI.

(5) Jain, P. K.; ElSayed, I. H.; El-Sayed, M. A. Au Nanoparticles Target Cancer. *Nano Today* **2007**, *2* (1), 18–29. https://doi.org/10.1016/S1748-0132(07)70016-6.

(6) Li, M.; Lohmü, T.; Feldmann, J. Optical Injection of Gold Nanoparticles into Living Cells. *Nano Lett* **2015**, *15* (1), 770–775. https://doi.org/10.1021/nl504497m.

(7) Gobin, A. M.; O'Neal, D. P.; Watkins, D. M.; Halas, N. J.; Drezek, R. A.; West, J. L. Near Infrared Laser-Tissue Welding Using Nanoshells as an Exogenous Absorber. *Lasers Surg. Med.* **2005**, *37* (2), 123–129. https://doi.org/10.1002/LSM.20206.

(8) Qiu, J.; David Wei, W. Surface Plasmon-Mediated Photothermal Chemistry. *J. Phys. Chem. C* **2014**, *118*, 20735–20749. https://doi.org/10.1021/jp5042553.

(9) Fang, Z.; Zhen, Y. R.; Neumann, O.; Polman, A.; García De Abajo, F. J.; Nordlander, P.; Halas, N. J. Evolution of Light-Induced Vapor Generation at a Liquid-Immersed Metallic Nanoparticle. *Nano Lett.* **2013**, *13* (4), 1736–1742. https://doi.org/10.1021/NL4003238/SUPPL_FILE/NL4003238_SI_002.AVI.

(10) Richardson, H. H.; Carlson, M. T.; Tandler, P. J.; Hernandez, P.; Govorov, A. O. Experimental and Theoretical Studies of Light-to-Heat Conversion and Collective Heating Effects in Metal Nanoparticle Solutions. *Nano Lett.* **2009**, *9* (3), 1139–1146. https://doi.org/10.1021/NL8036905/ASSET/IMAGES/LARGE/NL-2008-036905_0005.JPEG.

(11) Ávalos-Ovando, O.; Besteiro, L. V.; Movsesyan, A.; Markovich, G.; Liedl, T.; Martens, K.; Wang, Z.; Correa-Duarte, M. A.; Govorov, A. O. Chiral Photomelting of DNA-Nanocrystal Assemblies Utilizing Plasmonic Photoheating. *Nano Lett.* **2021**, *21* (17), 7298–7308. https://doi.org/10.1021/ACS.NANOLETT.1C02479/ASSET/IMAGES/LARGE/NL1C02479_0005.JPEG.

(12) Lu, J.; Choi, E.; Tamanoi, F.; Zink, J. I.

Light-Activated Nanoimpeller-Controlled Drug Release in Cancer Cells. *Small* **2008**, *4* (4), 421–426. https://doi.org/10.1002/SMLL.200700903.

(13) Reisner, W.; Larsen, N. B.; Silahtaroglu, A.; Kristensen, A.; Tommerup, N.; Tegenfeldt, J. O.; Flyvbjerg, H. Single-Molecule Denaturation Mapping of DNA in Nanofluidic Channels. *Proc. Natl. Acad. Sci. U. S. A.* **2010**, *107* (30), 13294–13299. https://doi.org/10.1073/PNAS.1007081107/-/DCSUPPLEMENTAL/PNAS.1007081107_SI.PDF.

(14) Zhang, X.; Chen, H.; Fu, H.; Doyle, P. S.; Yan, J. Two Distinct Overstretched DNA Structures Revealed by Single-Molecule Thermodynamics Measurements. *Proc. Natl. Acad. Sci. U. S. A.* **2012**, *109* (21), 8103–8108. https://doi.org/10.1073/PNAS.1109824109/-/DCSUPPLEMENTAL/APPENDIX.PDF.

(15) Williams, M. C.; Wenner, J. R.; Rouzina, I.; Bloomfield, V. A. Entropy and Heat Capacity of DNA Melting from Temperature Dependence of Single Molecule Stretching. *Biophys. J.* **2001**, *80* (4), 1932–1939. https://doi.org/10.1016/S0006-3495(01)76163-2.

(16) Stephenson, W.; Keller, S.; Santiago, R.; Albrecht, J. E.; Asare-Okai, P. N.; Tenenbaum, S. A.; Zuker, M.; Li, P. T. X. Combining Temperature and Force to Study Folding of an RNA Hairpin. *Phys. Chem. Chem. Phys.* **2013**, *16* (3), 906–917. https://doi.org/10.1039/C3CP52042K.

(17) Zhao, R.; Marshall, M.; Alemán, E. A.; Lamichhane, R.; Feig, A.; Rueda, D. Laser-Assisted Single-Molecule Refolding (LASR). *Biophys. J.* **2010**, *99* (6), 1925–1931. https://doi.org/10.1016/J.BPJ.2010.07.019.

(18) Ishijima, A.; Yanagida, T. Single Molecule Nanobioscience. *Trends Biochem. Sci.* **2001**, *26* (7), 438–444. https://doi.org/10.1016/S0968-0004(01)01860-6.

(19) Bustamante, C.; Bryant, Z.; Smith, S. B. Ten Years of Tension: Single-Molecule DNA Mechanics. *Nat. 2003 4216921* **2003**, *421* (6921), 423–427. https://doi.org/10.1038/nature01405.

(20) Fiore, J. L.; Kraemer, B.; Koberling, F.; Edmann, R.; Nesbitt, D. J. Enthalpy-Driven RNA Folding: Single-Molecule Thermodynamics of Tetraloop-Receptor Tertiary Interaction. *Biochemistry* **2009**, *48* (11), 2550–2558. https://doi.org/10.1021/BI8019788/SUPPL_FILE/BI8019788_SI_001.PDF.

(21) Holmstrom, E. D.; Fiore, J. L.; Nesbitt, D. J. Thermodynamic Origins of Monovalent Facilitated RNA Folding. *Biochemistry* **2012**, *51* (18), 3732–3743. https://doi.org/10.1021/BI201420A/SUPPL_FILE/BI201420A_SI_004.PDF.

(22) Zhou, Y.; Tang, Q.; Zhao, X.; Zeng, X.; Chong, C.; Yan, J. A Novel Design for Magnetic Tweezers with Wide-Range Temperature Control. *Biophys. J.* **2023**, *122* (19), 3860–3868. https://doi.org/10.1016/j.bpj.2023.08.004.

(23) Holmstrom, E. D.; Nesbitt, D. J. Real-Time Infrared Overtone Laser Control of Temperature in Picoliter H 2 O Samples: “Nanobathtubs” for Single Molecule Microscopy. *J. Phys. Chem. Lett* **2010**, *1*, 53. https://doi.org/10.1021/jz100663e.

(24) Slyadnev, M. N.; Tanaka, Y.; Tokeshi, M.; Kitamori, T. Photothermal Temperature Control of a Chemical Reaction on a Microchip Using an Infrared Diode Laser. *Anal. Chem.* **2001**, *73* (16), 4037–4044.

https://doi.org/10.1021/AC010318P.

(25) Mao, H.; Arias-Gonzalez, J. R.; Smith, S. B.; Tinoco, I.; Bustamante, C. Temperature Control Methods in a Laser Tweezers System. *Biophys. J.* **2005**, *89* (2), 1308–1316. https://doi.org/10.1529/BIOPHYSJ.104.054536.

(26) Peterman, E. J. G.; Gittes, F.; Schmidt, C. F. Laser-Induced Heating in Optical Traps. *Biophys. J.* **2003**, *84* (2 I), 1308–1316. https://doi.org/10.1016/S0006-3495(03)74946-7.

(27) De Lorenzo, S.; Ribezzi-Crivellari, M.; Arias-Gonzalez, J. R.; Smith, S. B.; Ritort, F. A Temperature-Jump Optical Trap for Single-Molecule Manipulation. *Biophys. J.* **2015**, *108* (12), 2854–2864. https://doi.org/10.1016/J.BPJ.2015.05.017.

(28) Holmstrom, E. D.; Dupuis, N. F.; Nesbitt, D. J. Pulsed IR Heating Studies of Single-Molecule DNA Duplex Dissociation Kinetics and Thermodynamics. *Biophys. J.* **2014**, *106* (1), 220–231. https://doi.org/10.1016/J.BPJ.2013.11.008.

(29) Zondervan, R.; Kulzer, F.; Van Der Meer, H.; Disselhorst, J. A. J. M.; Orrit, M. Laser-Driven Microsecond Temperature Cycles Analyzed by Fluorescence Polarization Microscopy. *Biophys. J.* **2006**, *90* (8), 2958–2969. https://doi.org/10.1529/BIOPHYSJ.105.075168.

(30) Yuan, H.; Xia, T.; Schuler, B.; Orrit, M. Temperature-Cycle Single-Molecule FRET Microscopy on Polyprolines. *Phys. Chem. Chem. Phys* **2011**, *13* (5), 1762–1769. https://doi.org/10.1039/c0cp01772h.

(31) Ferdinandus; Suzuki, M.; Quang Vu, C.; Harada, Y.; Ranjan Sarker, S.; Ishiwata, S.; Kitaguchi, T.; Arai, S. Modulation of Local Cellular Activities Using a Photothermal Dye-Based Subcellular-Sized Heat Spot. *ACS Nano* **2022**, *16* (6), 9004–9018. https://doi.org/10.1021/acsnano.2c00285.

(32) Turek, V. A.; Chikkaraddy, R.; Cormier, S.; Stockham, B.; Ding, T.; Keyser, U. F.; Baumberg, J. J.; Turek, V. A.; Chikkaraddy, R.; Cormier, S.; Stockham, B.; Ding, T.; Keyser, U. F.; Baumberg, J. J. Thermo-Responsive Actuation of a DNA Origami Flexor. *Adv. Funct. Mater.* **2018**, *28*, 1706410. https://doi.org/10.1002/adfm.201706410.

(33) Cormier, S.; Ding, T.; Turek, V.; Baumberg, J. J. Actuating Single Nano-Oscillators with Light. *Adv. Opt. Mater.* **2018**, *6* (6), 1701281. https://doi.org/10.1002/ADOM.201701281.

(34) Ding, T.; Valev, V. K.; Salmon, A. R.; Forman, C. J.; Smoukov, S. K.; Scherman, O. A.; Frenkel, D.; Baumberg, J. J. Light-Induced Actuating Nanotransducers. *Proc. Natl. Acad. Sci. U. S. A.* **2016**, *113* (20), 5503–5507. https://doi.org/10.1073/PNAS.1524209113/SUPPL_FILE/PNAS.1524209113.SAPP.PDF.

(35) Jain, P. K.; Lee, K. S.; El-Sayed, I. H.; El-Sayed, M. A. Calculated Absorption and Scattering Properties of Gold Nanoparticles of Different Size, Shape, and Composition: Applications in Biological Imaging and Biomedicine. *J. Phys. Chem. B* **2006**, *110* (14), 7238–7248. https://doi.org/10.1021/JP057170O/ASSET/IMAGES/LARGE/JP057170OF00006.JPEG.

(36) Storhoff, J. J.; Elghanian, R.; Mirkin, C. A.; Letsinger, R. L. Sequence-Dependent Stability of DNA-Modified Gold Nanoparticles. *Langmuir* **2002**, *18*, 6666–

6670. https://doi.org/10.1021/la0202428.

(37) Zhao, Z.; Jacovetty, E. L.; Liu, Y.; Yan, H. Encapsulation of Gold Nanoparticles in a DNA Origami Cage. *Angew. Chemie Int. Ed.* **2011**, *50* (9), 2041–2044. https://doi.org/10.1002/ANIE.201006818.

(38) Kuzyk, A.; Schreiber, R.; Zhang, H.; Govorov, A. O.; Liedl, T.; Liu, N. Reconfigurable 3D Plasmonic Metamolecules. *Nat. Mater.* **2014**, *13* (9), 862–866. https://doi.org/10.1038/nmat4031.

(39) Schreiber, R.; Santiago, I.; Ardavan, A.; Turberfield, A. J. Ordering Gold Nanoparticles with DNA Origami Nanoflowers. *ACS Nano* **2016**, *10* (8), 7303–7306. https://doi.org/10.1021/ACSNANO.6B03076/SUPPL_FILE/NN6B03076_SI_001.PDF.

(40) Kuzyk, A.; Schreiber, R.; Fan, Z.; Pardatscher, G.; Roller, E.-M.; Högele, A.; Simmel, F. C.; Govorov, A. O.; Liedl, T. DNA-Based Self-Assembly of Chiral Plasmonic Nanostructures with Tailored Optical Response. *Nature* **2012**, *483(7389),311-314*. https://doi.org/10.1038/nature10889.

(41) Bustamante, C.; Smith, S. B.; Liphardt, J.; Smith, D. Single-Molecule Studies of DNA Mechanics. *Curr. Opin. Struct. Biol.* **2000**, *10* (3), 279–285. https://doi.org/10.1016/S0959-440X(00)00085-3.

(42) Darcy, M.; Crocker, K.; Wang, Y.; Le, J. V.; Mohammadiroozbahani, G.; Abdelhamid, M. A. S.; Craggs, T. D.; Castro, C. E.; Bundschuh, R.; Poirier, M. G. High-Force Application by a Nanoscale DNA Force Spectrometer. *ACS Nano* **2022**, *16* (4), 5682–5695. https://doi.org/10.1021/ACSNANO.1C10698/ASSET/IMAGES/MEDIUM/NN1C10698_M022.GIF.

(43) Guglielmelli, A.; Pierini, F.; Tabiryan, N.; Umeton, C.; Bunning, T. J.; Sio, L. De. Thermoplasmonics with Gold Nanoparticles: A New Weapon in Modern Optics and Biomedicine. *Adv. Photonics Res.* **2021**, *2* (8), 2000198. https://doi.org/10.1002/ADPR.202000198.

(44) Pratt, J. W.; Gibbons, J. D. Kolmogorov-Smirnov Two-Sample Tests, *Concepts of Non-parametric Theory, Springer Series in Statistics, Springer, New York, NY,* 1981; pp 318–344.

(45) Lang, M. J.; Fordyce, P. M.; Fordyce, A. M.; Neuman, K. C.; Block, S. M. Simultaneous, Coincident Optical Trapping and Single-Molecule Fluorescence. *Nat. Methods 2004 12* **2004**, *1* (2), 133–139. https://doi.org/10.1038/nmeth714.

(46) Johnson, J. A.; Dehankar, A.; Winter, J. O.; Castro, C. E. Reciprocal Control of Hierarchical DNA Origami-Nanoparticle Assemblies. *Nano Lett* **2019**, *19*, 8469-8475. https://doi.org/10.1021/acs.nanolett.9b02786.

(47) Zhuang, X.; Rief, M. Single-Molecule Folding. *Curr. Opin. Struct. Biol.* **2003**, *13* (1), 88–97. https://doi.org/10.1016/S0959-440X(03)00011-3.

(48) Kruithof, M.; Chien, F.; De Jager, M.; Van Noort, J. Subpiconewton Dynamic Force Spectroscopy Using Magnetic Tweezers. *Biophys. J.* **2008**, *94* (6), 2343–2348. https://doi.org/10.1529/BIOPHYSJ.107.121673.

(49) Hansma, H. G.; Laney, D. E.; Bezanilla, M.; Sinsheimer, R. L.; Hansma, P. K. Applications for Atomic Force Microscopy of DNA. *Biophys. J.* **1995**, *68*

(5), 1672–1677.
https://doi.org/10.1016/S0006-3495(95)80343-7.

TOC Graphic

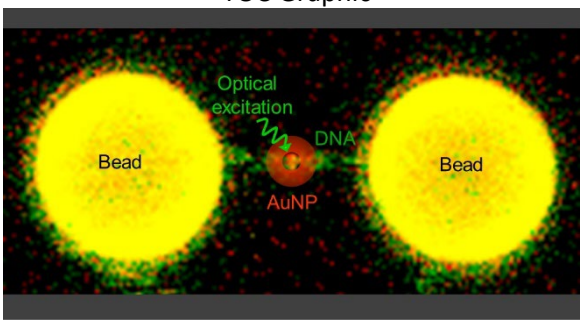

Localized plasmonic heating for single-molecule DNA rupture measurements in optical tweezers

Prerna Kabtiyal[1], Ariel Robbins[2], Elizabeth Jergens[2], Carlos E. Castro[2,3], Jessica O. Winter[2,4], Michael G. Poirier[1,2,5]*, Ezekiel Johnston-Halperin[1]**

[1]Department of Physics, The Ohio State University, Columbus, Ohio-43210, USA

[2] Biophysics Graduate Program, The Ohio State University, Columbus, Ohio-43210, USA

[3] Department of Mechanical and Aerospace Engineering, The Ohio State University, Columbus, Ohio-43210, USA

[4]Department of Chemical and Biomolecular Engineering, The Ohio State University, Columbus, Ohio-43210, USA

[5]Department of Chemistry and Biochemistry, The Ohio State University, Columbus, Ohio-43210, USA

*poirier.18@osu.edu , **johnston-halperin.1@osu.edu

Supplementary 1: Calculation of incident intensities for the two wavelengths, and calculation of temperature dependent reaction coordinates from Arrhenius equation.

Calculation of incident intensities for different wavelengths

The total available intensities (I_{inc}) for the two wavelengths (i.e. 561 nm and 639 nm) are calculated using the intensity equation for a gaussian beam as shown below,

$$I_{inc} = \frac{2 \times Incident\ Power}{Area\ of\ laser\ spot} \qquad (i)$$

The intensities are calculated to be $I^{max}_{561nm} = 16.4\text{x}10^{-4}\ \mu\text{Wnm}^{-2}$ ($P^{max}_{561nm} = 47.9\ \mu\text{W}$, spot $size_{561nm}$= X:295 nm, Y:251 nm) and $I^{max}_{639nm} = 14.6\text{x}10^{-4}\ \mu\text{Wnm}^{-2}$ ($P^{max}_{639nm} = 47.9\ \mu\text{W}$, spot $size_{639nm}$= X:304 nm, Y:265 nm).

Calculation of temperature dependent reaction coordinate for dark and excited rupture

The temperature dependence of the reaction-coordinate 'd' was studied using the comparison between plasmonically excited and non-excited shear-induced rupture of the DNA-Au-DNA constructs at three different shear forces, i.e., 2.5 pN, 5 pN, and 10 pN. For this the obtained rupture data was fit to the logarithmic form of the Arrhenius equation described as,

$$\ln(k) = (ln\, k_0 - \frac{\Delta G}{k_B T}) + \frac{Fd}{k_B T} \qquad (ii)$$

where k is the reaction constant for the rupture, k_0 is the Arrhenius constant, ΔG is the Gibbs energy cost of reaching the transition state, F is the Force applied, d is the reaction-coordinate, k_B is the Boltzmann constant, and T is the temperature.

The reaction constant k was calculated for each applied force using the temporally binned cumulative probability of the observed rupture events with bin size=30 s, only plotted for bins that contribute to an increase in the rupture events. This plot is fitted to the function

($1-e^{-kx}$) as shown in figure S1 to obtain the reaction constant '*k'* for dark and excited rupture at each force. The natural logarithm of the rate constants for dark and excited rupture are then plotted as a function of applied force as shown in figure S2. According to the above equation, this plot should be a linear relationship with the slope given by d/k_BT, and therefore if the temperature is known then the value of the reaction coordinate can be extracted.

The calculated slopes for the dark and excited ruptures are (0.15 ± 0.04) pN^{-1} and (0.3 ± 0.15) pN^{-1} respectively (Fig. S2). The room temperature during dark excitation is considered to be T_{Dark} = 25 °C to calculate d_{Dark} = (0.62 ± 0.16) nm. For the excited rupture the calculated average temperature $T_{Excited}$ = 34.1 °C is used (calculated along the maximum range of construct attachment from the AuNP surface) to calculate a $d_{Excited}$ = (1.37 ± 0.69) nm. This shows that the value of the reaction constant roughly doubled for excited rupture when compared to dark rupture.

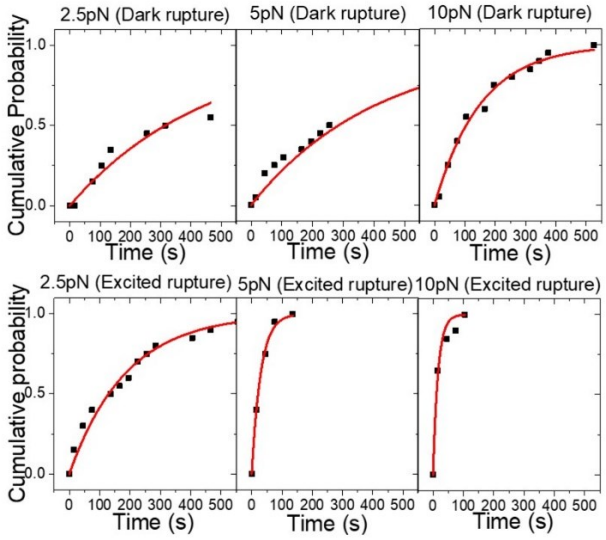

Fig S1: Curve fit of the observed cumulative probability of rupture to extract the rate constant of rupture at each shear force for dark rupture (upper panel) and excited rupture(lower panel).

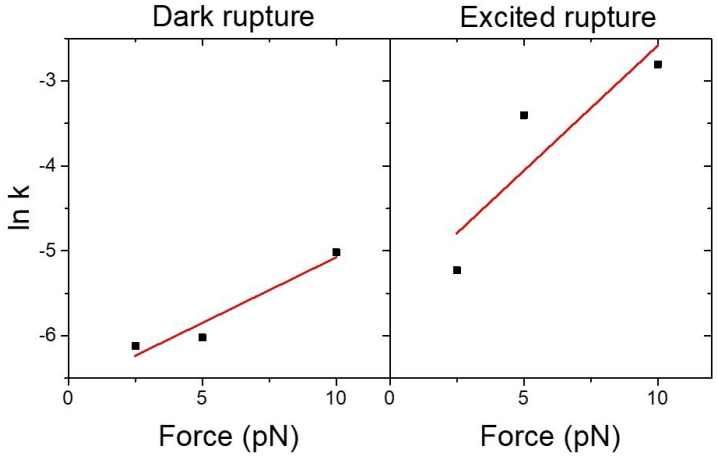

Fig S2: Plot of natural log of reaction constant 'k' versus the applied shear force. Linear curve fit is performed for dark and excited rupture to calculate the slope to further obtain reaction coordinate 'd'.